Applied Catalysis B: Environmental 337 (2023) 122956

Contents lists available at ScienceDirect

Applied Catalysis B: Environmental

journal homepage: www.elsevier.com/locate/apcatb

Atomic layer deposited platinum on tungsten oxide support as high performance hybrid catalysts for polymer electrolyte membrane fuel cells

Hae Wook Park [a,1], Beum Geun Seo [b,1], Jung Woo Shim [b], Nam Il Kim [a], Yun Sung Choi [b], Joon Hyung Shim [a,b,*]

[a] Department of Automotive Convergence, Korea University, Republic of Korea
[b] School of Mechanical Engineering, Korea University, Republic of Korea

ARTICLE INFO

Keywords:
PEMFC catalyst support
FCEV driving conditions
Tungsten oxide
Atomic layer deposition
Reversal-tolerant anode

ABSTRACT

Under actual fuel cell electric vehicle operation with various harsh conditions, polymer electrolyte membrane fuel cells exhibit significantly reduced performance owing to the carbon support corrosion. To overcome these limitations, this study used WO_3 as an anode catalyst support. Tungsten oxide can supply additional hydrogen ions and electrons via the decomposition of tungsten bronze (H_xWO_3) produced by the hydrogen spillover effect. Furthermore, H_xWO_3 also stabilizes the cell potential by scavenging oxygen infiltrated into the anode during start-up/shut-down situations. However, the initial performance degradation can be induced by the low electrical conductivity of the metal oxide. To compensate for this, Ar plasma surface treatment was performed on the WO_3 layer, and Pt nanoparticles were formed through atomic layer deposition to manufacture an extremely robust anode catalyst. Ultimately, it showed noticeably enhanced durability in diverse operating conditions compared to the commercial Pt/C and even displayed the effect as a reversal-tolerant anode.

1. Introduction

Fuel cell electric vehicles (FCEVs) are gaining attention as next-generation transportation methods owing to their environmental friendliness, rapid charging time, and long mileage per charge [1–3]. In particularly, because hydrogen fuel has a higher energy density than lithium-ion batteries (H_2: 130 MJ/kg, Li-ion battery: 0.7 MJ/kg), it is expected to quickly replace long-distance heavy-duty transport vehicles with serious pollution issues [4,5]. Additionally, polymer electrolyte membrane fuel cells (PEMFCs) are anticipated to be in great demand for large vehicles, because commercial vehicles are less burdened with building a hydrogen charging infrastructure [6]. Considering that platinum catalysts account for approximately 40 % of the production cost for these PEMFCs, it is no exaggeration to say that the key to commercializing large FCEV is reducing platinum usage [7–9]. Moreover, to enhance the long-distance transport ability and loading capacity, it is essential to guarantee the long-term operational durability of the catalyst [10–12].

In real FCEV operation, the deterioration of the PEMFC membrane electrode assembly (MEA) can be accelerated under repeated start-up/shut-down (SU/SD) environments and fuel starvation conditions [13–17]. The principal cause of this degradation is the corrosion of carbon black, which is a Pt/C catalyst support. More specifically, when the PEMFC is subjected to an excessive load change and a hydrogen fuel shortage momentarily occurs in the stack, the anode carbon support reacts with water to meet the required power [18,19]. During the SU/SD cycles, the chemical potential of the cathode briefly surpasses 1.5 V owing to anode air penetration, which increases cathode corrosion by exposing the carbon support to the oxidizing environment [16,20–22]. As a result, the Pt catalyst particles detach from the carbon support and undergo a process known as Ostwald ripening, in which the dissolved fine particles agglomerate with nearby large particles [23,24]. This causes Pt catalysts to gradually aggregate into giant particles. Ultimately, the electrochemical reaction sites are diminished along with a significant reduction in the triple-phase boundaries, and it becomes difficult to deliver reactants because of the physical coverage of the massive particles [25,26].

Therefore, numerous experiments have been conducted to develop supports with corrosion resistance [27–31]. Although carbon nanotubes (CNTs), graphene, and other graphitized materials with more stable

* Corresponding author at: School of Mechanical Engineering, Department of Automotive Convergence, Korea University, Republic of Korea.
E-mail address: shimm@korea.ac.kr (J.H. Shim).
[1] These authors contributed equally to this work.

https://doi.org/10.1016/j.apcatb.2023.122956
Received 6 February 2023; Received in revised form 21 May 2023; Accepted 3 June 2023
Available online 5 June 2023

structures than carbon black have been used, they have not yet provided a fundamental solution to carbon corrosion [32,33]. Accordingly, attempts to replace the support with metal oxides such as TiO_2, SnO_2, and MoO_2, which have strong stability in acidic environments are increasing [34–39]. A drawback of using metal oxides on electrodes is the decrease in the initial performance owing to poor electrical conductivity [33]. Research employing doped conductive oxides or carbon-mixed oxides to address this problem is ongoing [40–44].

In this study, tungsten oxide (WO_3) was used as a support for a Pt catalyst. WO_3 is an abundant material on Earth that exhibits a certain degree of electrical conductivity [45]. In addition, when the appropriate processing is performed, it possesses excellent conductivity, similar to that of a semi-conductor [46,47]. In particular, WO_3 is expected to operate synergistically when paired with Pt [48]. Hydrogen gas is divided into hydrogen ions and electrons in a Pt anode catalyst. If WO_3 is present, a reversible hydrogen spillover reaction occurs, in which H_xWO_y-type tungsten bronze is generated [48–53].

$$\text{Hydrogen spillover } \textit{effect} : WO_y + xH^+ + xe^- \leftrightarrow H_xWO_y$$

Because this tungsten bronze can behave as a hydrogen reservoir, when a scarcity of hydrogen occurs, as shown in Fig. 1, its capability to cope with power demand is improved through a reverse reaction.

$$O_2 \text{ scavenger} : 4H_xWO_y + xO_2 \rightarrow 4WO_y + 2xH_2O$$

Additionally, as indicated above, it also scavenges extra oxygen that has entered or crossed into the anode, resulting in cell potential stabilization and cathode corrosion prevention [13].

The conductivity of WO_3, which has several advantages in terms of endurance, was boosted by Ar plasma surface treatment, which was named P-WO_3 [54–56]. The density of electrons that function as charge carriers is increased by oxygen vacancies created by plasma treatment, making n-doped conduction feasible [57]. Next, Pt nano-catalysts were placed on the P-WO_3 support using atomic layer deposition (ALD). ALD is a subclass of chemical vapor deposition, a technology that enables the controlled deposition of materials in atomic units while managing their composition and size from self-limiting reactions between the precursor and reactant [58]. In particular, plasma-enhanced atomic layer deposition (PEALD) has the benefit of obtaining high-purity metals even at low temperatures using highly reactive plasma as a reactant [59,60]. This PEALD method allowed the uniform distribution of Pt at the nanoscale, and the catalytic activity was maximized with a small amount of precious metal [61]. The PEALD Pt/P-WO_3 catalyst synthesized in this manner was examined in terms of its fuel cell performance and durability in the MEA form.

2. Results and discussion

2.1. Electrically enhanced WO_3 layer by Ar plasma surface treatment

The WO_3 film produced by bar coating is shown in Fig. 2c. If the layer is excessively thick, it is difficult to obtain an effective hydrogen spillover phenomenon owing to ion trapping; therefore, the target thickness was set to 1–2 μm. After thickness optimization, we investigated the effect of Ar plasma surface treatment on the WO_3 film. Chemical changes following plasma treatment were observed by X-ray photoelectron spectroscopy (XPS). Fig. 2a, b and d show the narrow-scan data of W 4 f. Notably, the ratio of W^{4+} and W^{5+} to W^{6+} increased as the plasma treatment proceeded. Fig. 2e shows a graph summarizing the area percentages of the W species, where a large amount of W^{6+} was converted into W^{4+} and W^{5+} after plasma treatment. In other words, because oxygen vacancies in the WO_3 lattice were created via plasma treatment, the number of W^{4+} and W^{5+} states increased [56,62].

The positive effect of the plasma treatment was revealed in the electrical conductivity measurements of the thin film with the 4-point probe method. As seen in Fig. 2f, the WO_3 support was able to achieve enhanced electrical conductivity by six orders of magnitude after 10 min plasma exposure. This was because the chemical bonding between tungsten and oxygen was broken by the Ar species, and the electrons

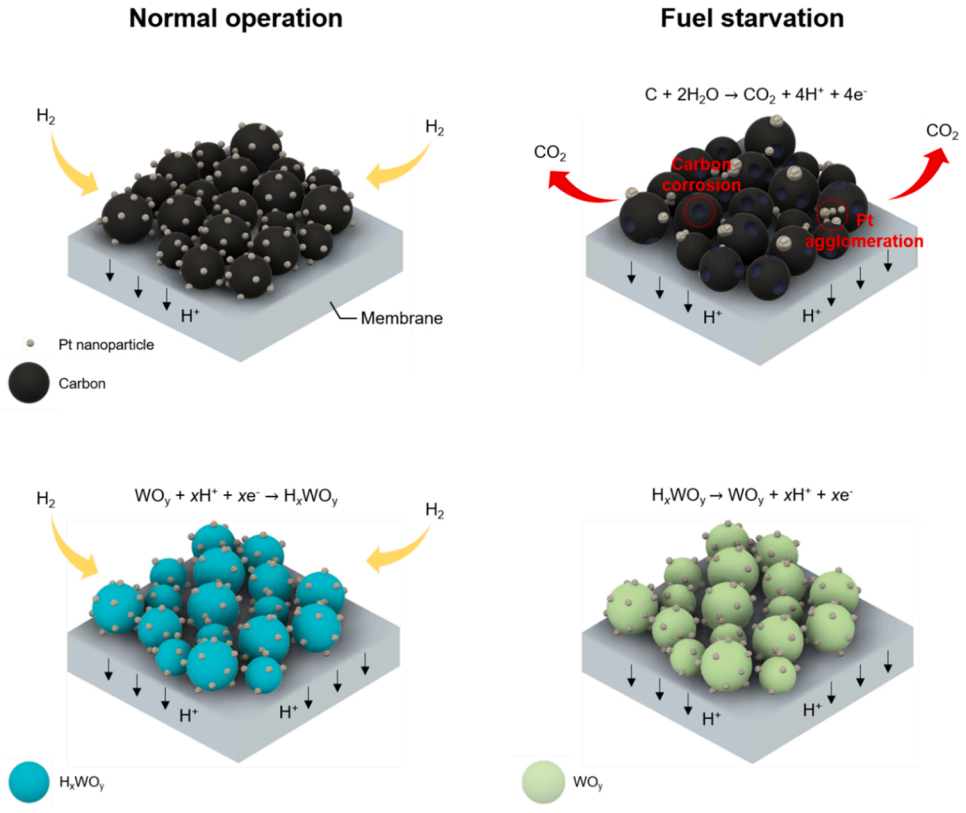

Fig. 1. Schematic design of processes occurring in PEMFC anode under normal operation and fuel starvation conditions. In Pt/C anodes, hydrogen ions and electrons are supplied through carbon corrosion reactions when hydrogen fuel is insufficient, which result in catalyst degradations. In contrast, Pt/WO_3 anodes produce H_xWO_y-type tungsten bronzes as a result of hydrogen spillover effect during normal operation. H_xWO_y generates the necessary hydrogen ions and electrons via a reverse reaction when hydrogen is not present.

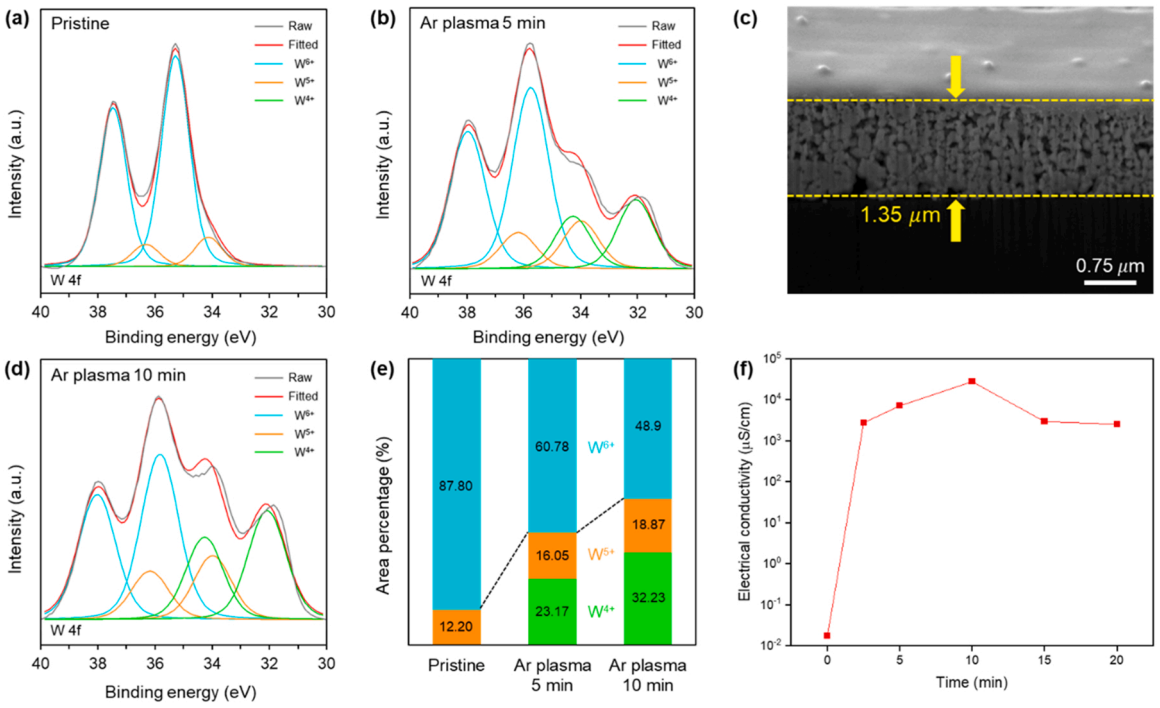

Fig. 2. Changes in bonding structure of the WO_3 layer and electrical conductivity improvement after Ar plasma treatment. XPS narrow scan profile of W 4 f following Ar plasma exposure time: (a) pristine, (b) 5 min, (d) 10 min; (e) Comparison of W^{4+}, W^{5+}, and W^{6+} ratio after Ar plasma treatment. (c) Finite ion beam (FIB) cross-sectional SEM image of the WO_3 layer. (f) Measured electrical conductivity with the 4-point probe method.

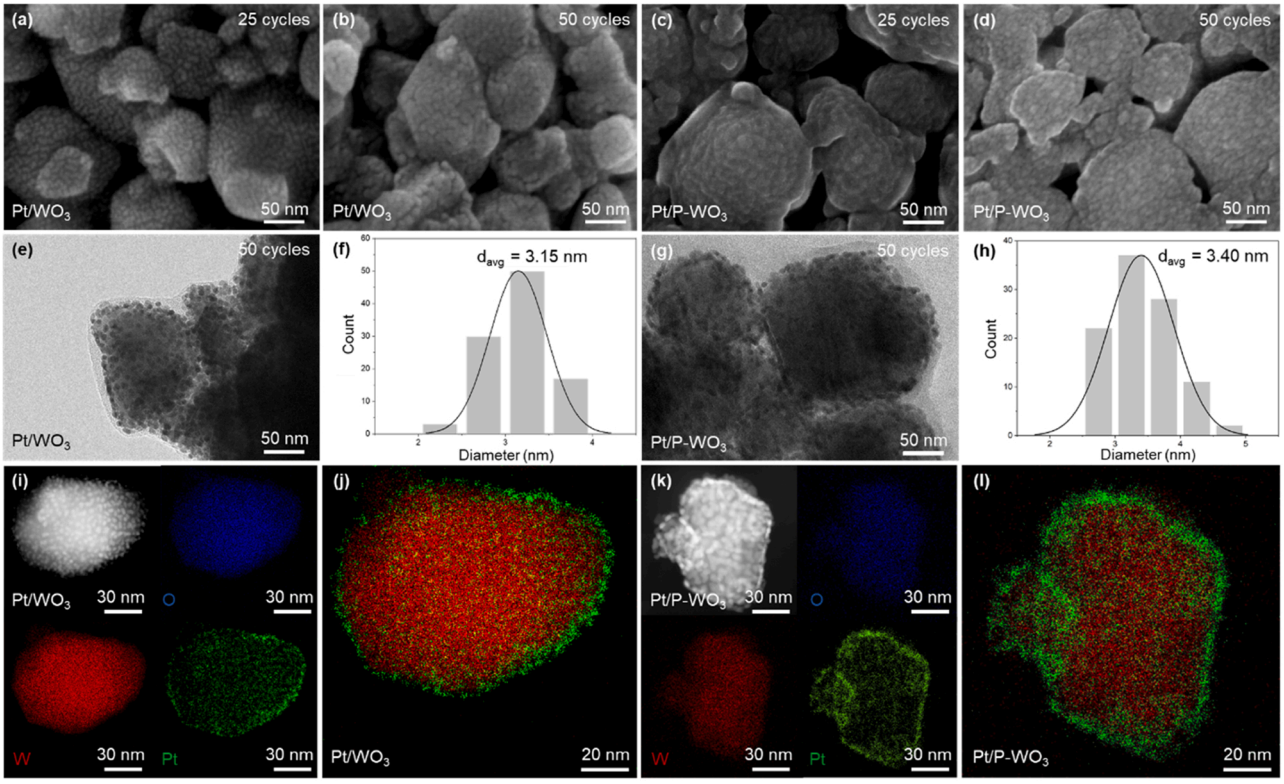

Fig. 3. Structure of the Pt/WO_3, $Pt/P\text{-}WO_3$ electrode. FE-SEM images of PEALD Pt on WO_3: (a) 25 cycles, (b) 50 cycles; (e) TEM image of Pt/WO_3 (PEALD Pt 50 cycles). (f) Particle size distribution of Pt/WO_3 TEM image (PEALD Pt 50 cycles). (i) EDS mapping data from STEM image of Pt/WO_3 catalyst (PEALD Pt 50 cycles). (j) Overlapping W and Pt elements in one image. FE-SEM images of PEALD Pt on Ar plasma pretreated WO_3: (c) 25 cycles, (d) 50 cycles; (g) TEM image of $Pt/P\text{-}WO_3$ (PEALD Pt 50 cycles). (h) Particle size distribution of $Pt/P\text{-}WO_3$ TEM image (PEALD Pt 50 cycles). (k) EDS mapping data from STEM image of $Pt/P\text{-}WO_3$ catalyst (PEALD Pt 50 cycles). (l) Overlapping W and Pt elements in one image.

that participated in the bonding behaved like free electrons in the film [63]. In other words, an increase in the Fermi level was induced by the generation of oxygen vacancies, and the WO_3 film had the same properties as an n-type semiconductor owing to the reduced band gap energy [54,64]. Therefore, it is demonstrated that Ar plasma surface treatment can be a solution to the escalation of cell electrical resistance, which is the biggest problem that arises when a metal oxide is applied as a support material.

2.2. Atomic layer deposited platinum on tungsten oxide support

The next step involved the formation of a Pt catalyst on the support. Therefore, as illustrated in Fig. S1, a high-purity PEALD Pt process tuned for a glass substrate was applied to the WO_3 support. Fig. 3a and b shows the field emission scanning electron microscope (FE-SEM) analysis data, and it is possible to observe the surface morphology of the Pt/WO_3 electrode. The Pt nanoparticles had an equivalent size distribution. When the number of PEALD cycles was increased, slightly enlarged Pt particles were observed. In other words, the PEALD technique enables uniformly distributed platinum particle deposition and nanoscale size control. Transmission electron microscopy (TEM) examination of the electrode also demonstrated that the catalyst synthesis was successful (Fig. 3e). Based on the TEM image, the average Pt particle size of the electrode conducting PEALD Pt 50 cycles was estimated using Image J (Fig. 3f). As a result, a size of approximately 3.15 nm was confirmed, which is comparable to the Pt particle size (2–3 nm) of the Pt/C electrode, therefore, the impact of morphological differences between the two electrodes was very limited [14]. It was reconfirmed that the nanoparticles uniformly deposited on the WO_3 support were Pt elements by energy dispersive spectroscopy (EDS) mapping of the PEALD Pt 50 cycles electrode scanning transmission electron microscopy (STEM) image (Fig. 3i and j).

We attempted to distinguish the changes in the electrode structure after PEALD of Pt on P-WO_3. Fig. 3c and d show the SEM image of Pt/P-WO_3, and it was found to have a flatter support surface compared with Fig. 3a and b. Additionally, when the same PEALD 50 cycles were performed, slightly larger Pt nanoparticles than that of the electrode without plasma treatment were created (Fig. 3 g and h). This means that Ar plasma was effective in improving the WO_3 surface reactivity because it directly broke the inert metal oxide state. Consequently, this could provide a more favorable environment for the adsorption of subsequent Pt precursors [65,66]. The initial Pt island formation was accelerated, and the grown Pt particles were uniformly distributed on the P-WO_3 as shown in Fig. 3k and l.

2.3. Improved PEMFC durability on harsh operating conditions

The prepared Pt/WO_3 electrode was applied to an MEA anode to evaluate its electrochemical performance. First, we attempted to accomplish optimal performance by controlling the number of Pt PEALD cycles. The test results obtained using the Pt/WO_3 anode without the Ar plasma treatment are shown in Fig. S2a, whereas Fig. S2b displays the outcomes of plasma treatment. By comparing these two graphs, the overall fuel cell output was enhanced. In particular, the slope of the I-V curves in the ohmic resistance region flattened, which was the positive effect of the improved electrical conductivity. Fig. S2a shows that a performance drop occurred after 100 cycles of PEALD Pt. A SEM image from Fig. S3 illustrates the primary reason for this phenomenon. Pt particles were overdeposited in response to excessive PEALD. Consequently, the electrochemical surface area (ECSA) of the catalyst decreased, and the mass transport of the reactant gas was hindered [67]. Similarly, Fig. S2b shows this behavior, but the impact is visible even on 75 cycles. As stated in the description above, this was generated by the Ar plasma treatment, which improved the WO_3 surface activity and increased the Pt particle size on average.

Among them, we chose PEALD Pt 50 cycles Pt/P-WO_3, which exhibited the highest performance and started a comparative verification with commercial Pt/C. Fig. 4a indicates that the gap could be reduced by more than half through Ar plasma treatment. In the 0.6 V region where the actual FCEV is driven, the power density showed a difference of 102 mW/cm^2 [68,69]. Furthermore, The HOR mass activity at 0.9 V also increased by approximately 71 % (Table. S1). This demonstrates that the ALD process also has an excellent effect at the MEA scale, showing the possibility of reducing the amount of precious metal catalysts.

However, because the physical properties of WO_3 are clearly distinct from those of the carbon black support, there was still dissidence in the formation of the triple-phase boundary where the actual catalytic reaction occurs. One of the variables that cause this difference is the surface area of the support [70,71]. Therefore, Brunauer-Emmett-Teller (BET) analysis was conducted to investigate the specific surface areas of WO_3 and carbon black. Fig. S4 shows the result. As can be seen from the isotherm plot, an interval between the two materials existed, and this resulted in 130 mW/cm^2 initial peak power density decrease. Because we did not proceed with the optimization for widening the WO_3 surface area in this research, it is possible to reduce the gap.

2.3.1. Hydrogen fuel starvation conditions

To induce a fuel starvation in PEMFC for actual driving conditions, an accelerated stress test was set in which the anode gas was converted into nitrogen under a constant current of 0.2 A/cm^2, purged for 30 s, and then converted back to hydrogen. As a result, the electrode using the P-WO_3 support maintained more than 98 % of its initial performance even after 4 cycles, whereas that of Pt/C electrode decreased by less than half (Fig. 4c). The peak power density was significantly lower than that of Pt/P-WO_3 after the test. This was because the tungsten oxide support had a resistance to corrosion and could accomplish 20 s longer voltage holding against the reverse voltage owing to the hydrogen spillover effect of WO_3. The changes in cell potential during one cycle of hydrogen shortage are shown in Fig. 4b. Although the holding time was not long, it was a very meaningful achievement because this situation occurs instantaneously during the PEMFC operation [18,72].

This delay was also proven to have a positive effect on the preservation of cell morphology, based on TEM analysis (Fig. 4 g and h). For the Pt/C electrode, detachment or agglomeration of Pt particles occurred much more severely because of the carbon corrosion.

2.3.2. FCEV acceleration conditions

The reverse voltage delay effect through the decomposition of hydrogen tungsten bronze is also shown in Fig. 4d. The experiments were conducted by simulating the rapid acceleration of an FCEV. The fuel supply was restricted to the level of 0.02 A/cm^2 and the cell load was switched to 1.0 A/cm^2 constant current. As in the previous experiments, approximately 15 s voltage holding was possible with the Pt/P-WO_3 electrode. Consequently, it was demonstrated that the WO_3 support also has the benefit of coping with transient power demand changes.

2.3.3. Reversal-tolerant anode effect

An interesting observation is revealed in Fig. 4e and f. By substituting nitrogen for the anode gas while maintaining current density at 0.2 A/cm^2, we measured the time for cell voltage to drop to −2 V. When the MEA experiences a voltage exceeding −2 V, electrolyte membrane breakdown and irreversible damage occur; therefore, only the time to reach that point was checked [18,73]. As shown in Fig. 4, the Pt/P-WO_3 anode accomplished approximately 38 min, which was more than 21 times that of Pt/C (105 s). Surprisingly, the voltage was maintained for a long time at approximately −1.8 V. This is because the separation rate of hydrogen tungsten bronze increased as the anode potential increased [74]. In previous studies, this reversal-tolerant anode (RTA) effect was obtained by adding an expensive water electrolysis catalyst such as IrO_x or RuO_x, but we were able to attain the same performance even with a less expensive WO_3 support [73,75–78].

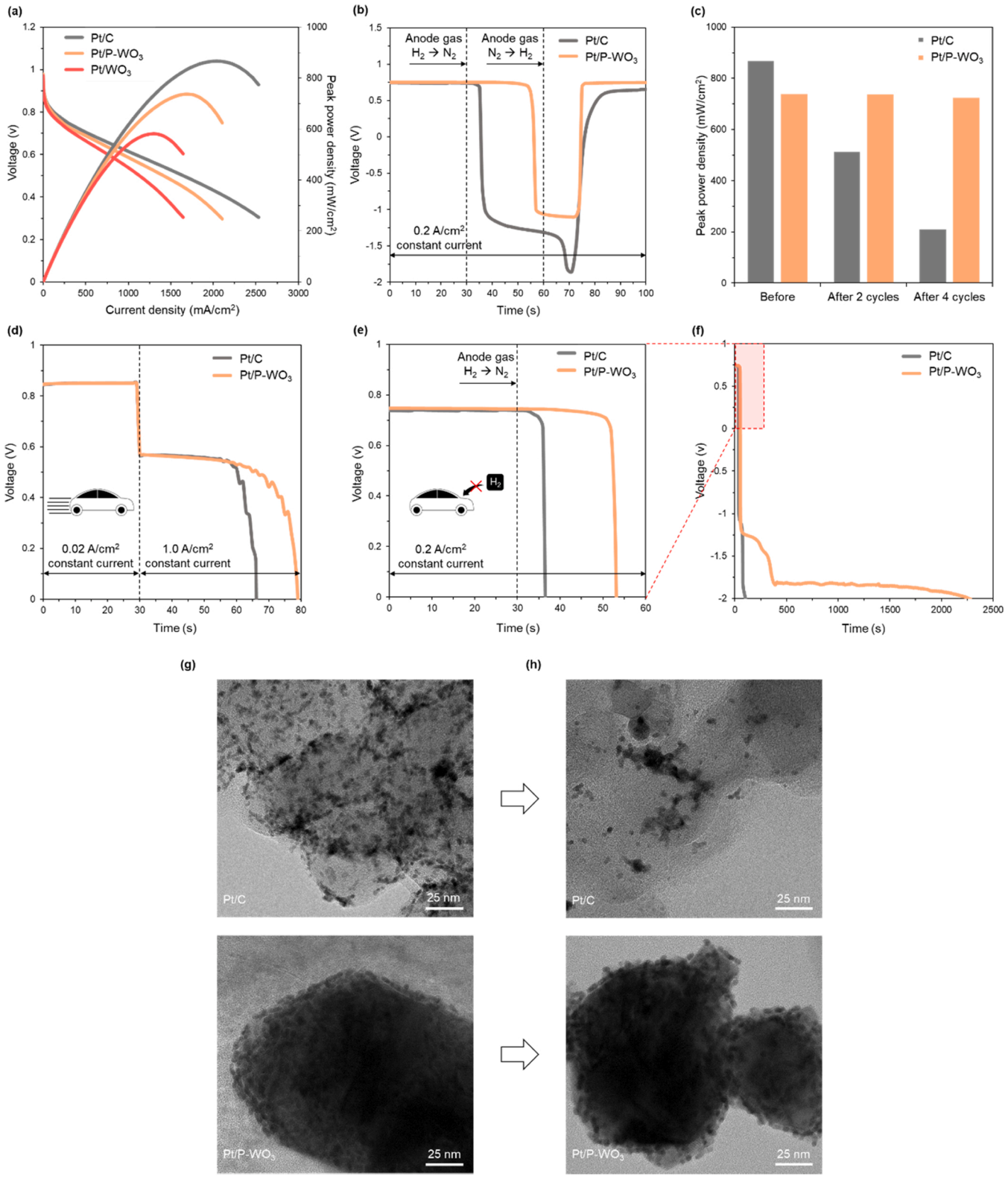

Fig. 4. Electrochemical performance under fuel starvation conditions. (a) Initial I-V performance of MEAs. (b) Comparison of cell voltage changes during fuel starvation durability tests. (c) Peak power density changes following fuel starvation durability tests. TEM images of the Pt/C and Pt/P-WO_3 anode before and after 4 cycles of MEA fuel starvation test: (g) Pt/C anode & Pt/P-WO_3 anode before, (h) Pt/C anode & Pt/P-WO_3 anode after; (d) Comparison of cell voltage changes on acceleration conditions (0.02 A/cm^2 → 1.0 A/cm^2) (e) Comparison of holding time for both MEAs to reach reverse voltage with switching anode gas from H_2 to N_2 at 30 s under constant current conditions. (f) Time measurement for both MEAs to reach −2 V with N_2 supply on the anode.

2.3.4. Operation with low humidified gas

The stability in a dry operating atmosphere was also investigated. Fig. 5 shows a graph in which the relative humidity (RH) of the supply gas was set to 30 % and cell degradation was observed while altering the necessary power value. When 5500 s had elapsed, it was determined that the electrode using Pt/C exhibited an entirely broken performance. In contrast, despite the occurrence of a reverse voltage, the Pt/P-WO_3 electrode did not show a total collapse. This resulted from the hydrophilic nature of tungsten oxide [79,80]. As shown in Table. S2, in which the contact angle between the two supports is compared, this improvement was realized by lessening the dry out damage of the membrane and ionomer owing to the more water-favorable WO_3 material. In addition, there was no evident distinction between the two electrodes when drive cycling was performed in 200 % RH environment.

2.3.5. Repetitive start-up/shut-down

The advantageous influence of the WO_3 support was also found in the durability test, assuming automobile start-up/shut-down (SU/SD) conditions. Fig. 6a displays the change in the peak power density after 10 cycles of the SU/SD test and reveals a better power retention of approximately 26 %. The same trend was observed in the electrochemical analysis results. When examining the changes in cathode ECSA through cyclic voltammetry (CV), it was possible to determine that the Pt/P-WO_3 anode outperformed the Pt/C anode in terms of preserving the activated surface area (Fig. 6b and f). The results of the normalized ECSA calculation based on these data are shown in Fig. 6e. Because the formed hydrogen tungsten bronze scavenged oxygen molecules in the air injected into the anode and stabilized its potential, the instantaneous increase in cathode potential was suppressed [13,14]. This O_2 capturing ability can be clearly observed in Fig. S5. As illustrated in the graph, when air was supplied instead of hydrogen, the cell potential gradually decreased, unlike that of Pt/C electrode. This effect can eventually minimize the oxygen reduction reaction (ORR) at the anode. Similar to CV, the change in charge transfer resistance in the electrochemical impedance spectroscopy (EIS) analysis showed a similar pattern (Fig. 6c and g). The unique point is that the use of Pt/C considerably increased the ohmic resistance. However, it remained nearly constant for Pt/P-WO_3. This phenomenon was feasible because the degree of membrane stimulation was controlled by preventing excessive elevation of the cathode potential. Additionally, the peroxide formation that occurs when the oxygen molecule encounters the hydrogen molecule at the anode was suppressed [81,82]. The comparison of the TEM images of each cathode after the SU/SD test also reinforces these conclusions (Fig. 6d and h).

3. Conclusion

In this study, we show that the initial performance degradation caused by the use of metal oxides could be compensated by the enhanced electrical conductivity through the Ar plasma surface treatment on the WO_3 layer. Furthermore, a hybrid catalyst was fabricated using the ALD technique, which achieved uniform Pt nanoparticle deposition on the support. By applying this Pt/P-WO_3 catalyst to the PEMFC MEA anode and conducting single cell tests that reflect actual FCEV driving conditions, Pt/P-WO_3 was found to be more durable than commercial Pt/C catalysts. In particular, it displayed RTA-like effects and elevated HOR mass activity. Based on these findings, it was demonstrated to be a successful anode catalyst for PEMFCs. This suggests the potential for developing fuel cell stacks that are resistant to corrosion based on non-carbon supports and minimizing the loading of platinum catalysts with restricted reserves. Ultimately, it is anticipated that the long-term driving capability of PEMFC will be guaranteed, which would accelerate the transition to the hydrogen era in automobiles and other applications.

4. Methods

4.1. Pt/P-WO_3 anode fabrication

A WO_3 slurry was produced by mixing 2000 mg of WO_3 nanopowder (Merck, Germany) and 4000 mg of anhydrous alcohol. The slurry was dispersed using tip sonicator (VCX 130, Sonics & Materials, USA) for 30 min and coated on a polyimide film with a height of 25 μm using a doctor-blade (KP-3000 V, Kipae, Republic of Korea). After drying in an oven at 70℃ for 24 h, the WO_3 film was subjected to reactive ion etching (RIE) (KVET-R4000, Korea Vacuum Tech, Republic of Korea) to conduct Ar plasma surface treatment. Ar (20 sccm) was injected into the chamber, which was set to a pressure of 30 mTorr, with an RF plasma power of 200 W.

In a custom-made PEALD (ICOT, Republic of Korea) chamber, the film was cut into 1.2 × 1.0 cm^2 specimens. A precursor pulse (1 s) - Ar purge (60 s) - O_2 plasma (15 s) - Ar purge (60 s) consisted of one cycle of PEALD and trimethyl(methylcyclopentadienyl)platinum(IV) ($MeCpPtMe_3$, Ichems, Republic of Korea) was used as the Pt precursor. The precursor was maintained at 70 ℃ and the deposition temperature was 150 ℃. O_2 (50 sccm) with an RF plasma power of 250 W was used to

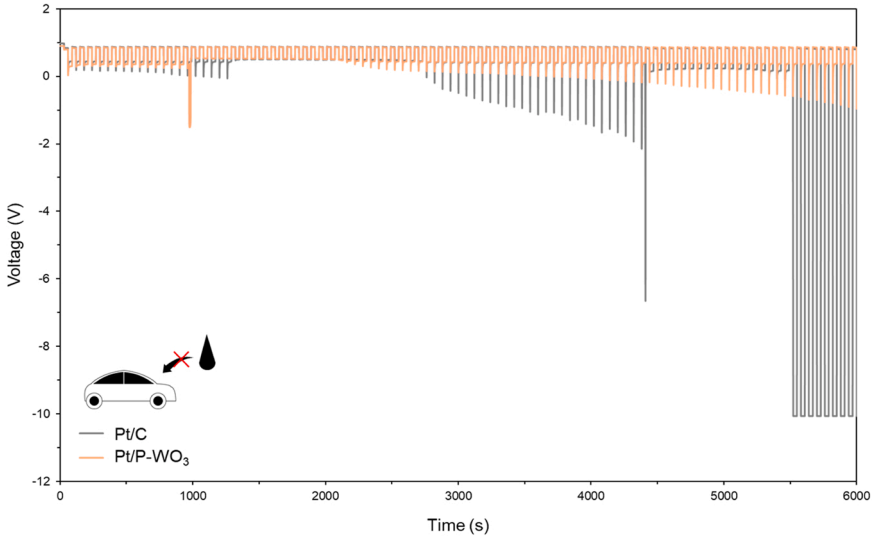

Fig. 5. Drive cycling (0.02 A/cm^2 ↔ 1.0 A/cm^2) durability test on dry conditions with relative humidity (RH) at 30 % H_2 and O_2 gas.

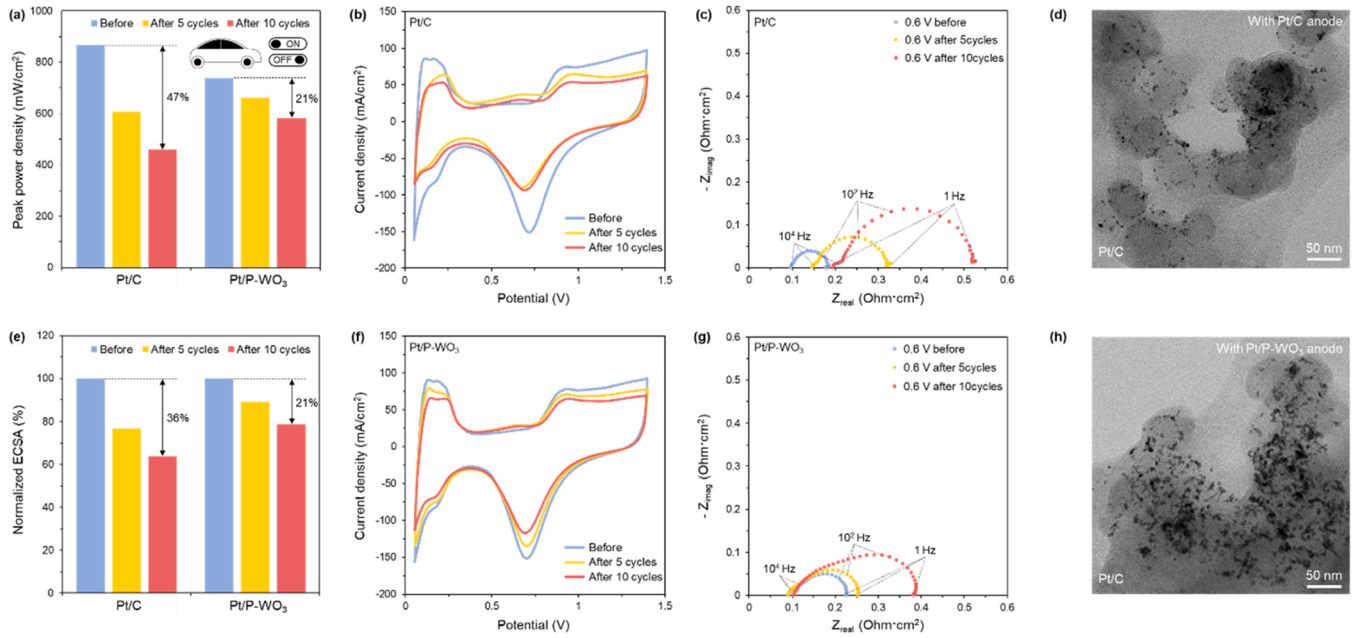

Fig. 6. Comparison of electrochemical performance under repetitive start-up/shut-down (SU/SD) conditions. (a) Peak power density changes following SU/SD cycles. (e) Normalized ECSA change following SU/SD cycles. In situ CV curves for SU/SD cycles: (b) MEA with the Pt/C anode, (f) MEA with the Pt/P-WO_3 anode; EIS curves for SU/SD cycles: (c) MEA with the Pt/C anode, (g) MEA with the Pt/P-WO_3 anode; TEM images of the Pt/C cathode after 10 cycles of MEA SU/SD test: (d) With the Pt/C anode, (h) With the Pt/P-WO_3 anode.

generate O_2 plasma. After Pt deposition, 40 μL of a 1:19 vol ratio solution with a 10 wt % water based Nafion ionomer (DuPont, USA) and ethanol was spread on the electrode using a micropipette. It was ten dried in an oven at 70 ℃ for 24 h.

4.2. MEA manufacture

The Pt/C electrode (for both the anode and cathode) was fabricated by bar coating on a polyimide film. A total of 530 mg of 40 wt % Pt/C (Alfa Aesar, USA), 2600 mg of a 10 wt % water based Nafion ionomer, and 8000 mg of isopropyl alcohol (IPA) were blended using a tip sonicator for 15 min. After coating the Pt/C slurry with a 150 μm blade height, the film was dried at 70 ℃for 24 h.

Before becoming a part of the MEA, all Pt/WO_3, Pt/P-WO_3, and Pt/C electrodes were cut to have a 0.85 × 0.95 cm^2 cell area. MEA was prepared by hot pressing (at 130 ℃and 380 kPa) electrodes on a Nafion 212 membrane (DuPont, USA). The synthesized MEA was combined with gas diffusion layers (GDLs) (Sigracet 39BB, SGL carbon, Germany) and bipolar plates.

4.3. Fuel cell test protocol

All tests were conducted on a fuel cell test station (CNL Energy, Republic of Korea) and ZIVE SP2 (WonATech, Republic of Korea) was used for the electrochemical performance measurements. Open circuit voltage (OCV) and I-V curves were obtained at a cell temperature of 60 ℃ under a H_2 (50 sccm)/O_2 (50 sccm) supply with RH 100 %. After checking the initial performance, the cells were subjected to various durability test conditions as follows (stoichiometry of H_2: 1.5/O_2: 4).

4.3.1. Fuel starvation

Anode gas was switched from H_2 (2 sccm) to N_2 (4 sccm) under 0.2 A/cm^2 constant current conditions (cathode gas: O_2 (2 sccm)). After 30 s of N_2 injection, the gas was again replaced with H_2 (2 sccm). Cell voltage changes during the cycles were observed and I-V curves were checked every two cycles.

4.3.2. Acceleration

To apply a transient load change, the H_2 supply was restricted to 2 sccm. The required current value was switched from 0.02 A/cm^2 to 1.0 A/cm^2. The cell voltage was recorded until it reached 0 V.

4.3.3. Reversal-tolerant anode

Similar to fuel starvation, N_2 (4 sccm) was supplied to the anode instead of H_2 (2 sccm) under 0.2 A/cm^2 constant current conditions. The time taken to reach 0 V and −2 V was recorded.

4.3.4. Drive cycling under dry conditions

RH 30 % H_2/O_2 gas flowed into the cell and the current value oscillated between 0.02 A/cm^2 and 1.0 A/cm^2 every 30 s. The test was continued for up to 6000 s

4.3.5. Start-up/shut-down

One cycle of SU/SD consisted of an OCV (30 s) - 0.4 A/cm^2 constant current (30 s) - anode air (30 sccm) injection under a 0.95 V constant voltage (15 s) - OCV. The anode gas was maintained at H_2 (3 sccm), except for air leakage, and the cathode gas was maintained at as O_2 (5 sccm). I-V curves, CV, and EIS were measured every five cycles.

4.4. Electrochemical analysis

The frequency sweep for EIS measurements was carried out from 10^7 Hz to 1 Hz with an applied AC amplitude of 10 mV and impedance data fitting was performed using Zman software (WonATech, Republic of Korea).

CV analysis was conducted after cell potential falling to 0.1 V by N_2 supply to the cathode. During the measurements, H_2 (100 sccm) and N_2 (5 sccm) were injected into the anode and cathode, respectively. The voltage sweep ranged from 0 V to 1.4 V with a 1 V/s scan rate. The ECSA was calculated from the hydrogen adsorption area of the CV graph (0.095–0.35 V) using the equation after double-layer adjustment.

4.5. Material and morphology characterization

Carbon black (Vulcan XC-72) for the control group was fabricated in the same way as the Pt/C electrode. 318 mg of carbon black powder (Alfa Aesar, USA), 2340 mg DI water and 8000 mg of IPA were blended using a tip sonicator for 15 min. After coating the slurry with a 150 μm blade height, the film was dried at 70 ℃ for 24 h.

The morphology of the electrodes was analyzed using FE-SEM (S-4800, HITACHI, Japan), TEM (NEO ARM, JEOL, Japan), and STEM (NEO ARM, JEOL, Japan). Furthermore, the thickness of the bar-coated layers was measured using FIB-SEM (LYRA3 XMH, TESCAN, Czech Republic).

The specific surface areas of the supports were compared by BET (3flex, Micromeritics, USA) data. BET surface area measurement was also carried out in the form of deposition on polyimide film. Total 28 × 30 cm^2 of deposited film was cut into 1 cm^2 based on the equipment specifications and used for the analysis.

The purity of PEALD Pt on glass and the change in W species on the WO_3 layer by Ar plasma treatment were checked by XPS (Nexsa, Thermo Fisher Scientific, USA). Electrical conductivity data were acquired using a 4-point probe system (M4P 302-System, MS-TECH, Republic of Korea), and ICP-OES (iCAP 6000 Series, Thermo Fisher Scientific, USA) analysis provided information about Pt loading on the electrodes.

CRediT authorship contribution statement

Hae Wook Park: Experiments, data curation, and writing – original draft preparation. **Beum Geun Seo**: Methodology, visualization and writing – review & editing. **Jung Woo Shim**: Methodology and investigation. **Nam Il Kim**: Experimental investigation. **Yun Sung Choi**: Data curation. **Joon Hyung Shim**: Conceptualization and supervision.

Declaration of Competing Interest

The authors declare that they have no known competing financial interests or personal relationships that could have appeared to influence the work reported in this paper.

Data availability

The data that has been used is confidential.

Acknowledgments

This work was supported by a National Research foundation of Korea (NRF, NRF-2019R1A2C2003054 and 2021M3I3A1084842) / a Korea institute of Energy Technology Evaluation and Planning (KETEP, 20213030030040) / Samsung Electronics.

Appendix A. Supporting information

Supplementary data associated with this article can be found in the online version at doi:10.1016/j.apcatb.2023.122956.

References

[1] D. Hu, Y. Wang, J. Li, Q. Yang, J. Wang, Investigation of optimal operating temperature for the PEMFC and its tracking control for energy saving in vehicle applications, Energy Conv. Manag. 249 (2021), 114842, https://doi.org/10.1016/j.enconman.2021.114842.

[2] Z. Bao, S. You, Z. Hu, Y. Wen, Coordinated operation of hydrogen refuelling and fast charging combo station under normal and contingent conditions, Energy Conv. Econ. 1 (2020) 171–183, https://doi.org/10.1049/enc2.12012.

[3] A. Perego, A. Avid, D.N. Mamania, Y. Chen, P. Atanassov, H. Yildirim, M. Odgaard IV, Zenyuk, Investigation of cathode catalyst layer interfacesd evolution during accelerated stress tests for polymer electrolyte fuel cells, Appl. Catal. B 301 (2022), 120810, https://doi.org/10.1016/j.apcatb.2021.120810.

[4] K.T. Møller, T.R. Jensen, E. Akiba, H.-W. Li, Hydrogen - a sustainable energy carrier, Prog. Nat. Sci. 27 (2017) 34–40, https://doi.org/10.1016/j.pnsc.2016.12.014.

[5] A. Kurzawski, L. Torres-Castro, R. Shurtz, J. Lamb, J.C. Hewson, Predicting cell-to-cell failure propagation and limits of propagation in lithium-ion cell stacks, Proc. Combust. Inst. 38 (2021) 4737–4745, https://doi.org/10.1016/j.proci.2020.06.270.

[6] X. Lü, Y. Qu, Y. Wang, C. Qin, G. Liu, A comprehensive review on hybrid power system for PEMFC-HEV: Issues and strategies, Energy Conv. Manag. 171 (2018) 1273–1291, https://doi.org/10.1016/j.enconman.2018.06.065.

[7] D. Bokach, S. ten Hoopen, N. Muthuswamy, M.E.M. Buan, M. Rønning, Nitrogen-doped carbon nanofiber catalyst for ORR in PEM fuel cell stack: Performance, durability and market application aspects, Int. J. Hydrog. 41 (2016) 17616–17630, https://doi.org/10.1016/j.ijhydene.2016.07.137.

[8] A. Ganesan, M. Narayanasamy, Ultra-low loading of platinum in proton exchange membrane-based fuel cells: a brief review, Mater. Renew. Sustain Energy 8 (2019) 18, https://doi.org/10.1007/s40243-019-0156-x.

[9] Y. Wu, M. Yuan, X. Li, R. Ding, X. Duan, J. Li, Y. Wang, X. Li, Y. Zhang, J. Liu, Assistance of rearrangement of active sites in Fe/N/C catalyst for harvesting ultra-high power density PEMFCs, Appl. Catal. B 312 (2022), 121365, https://doi.org/10.1016/j.apcatb.2022.121365.

[10] R.L. Borup, A. Kusoglu, K.C. Neyerlin, R. Mukundan, R.K. Ahluwalia, D.A. Cullen, K.L. More, A.Z. Weber, D.J. Myers, Recent developments in catalyst-related PEM fuel cell durability, Curr. Opin. Electrochem. 21 (2020) 192–200, https://doi.org/10.1016/j.coelec.2020.02.007.

[11] X. Yu, S. Ye, Recent advances in activity and durability enhancement of Pt/C catalytic cathode in PEMFC: Part II: Degradation mechanism and durability enhancement of carbon supported platinum catalyst, J. Power Sources 172 (2007) 145–154, https://doi.org/10.1016/j.jpowsour.2007.07.048.

[12] J. Wu, X.Z. Yuan, J.J. Martin, H. Wang, J. Zhang, J. Shen, S. Wu, W. Merida, A review of PEM fuel cell durability: degradation mechanisms and mitigation strategies, J. Power Sources 184 (2008) 104–119, https://doi.org/10.1016/j.jpowsour.2008.06.006.

[13] G. Shen, J. Liu, H.B. Wu, P. Xu, F. Liu, C. Tongsh, K. Jiao, J. Li, M. Liu, M. Cai, J. P. Lemmon, G. Soloveichik, H. Li, J. Zhu, Y. Lu, Multi-functional anodes boost the transient power and durability of proton exchange membrane fuel cells, Nat. Commun. 11 (2020) 1191, https://doi.org/10.1038/s41467-020-14822-y.

[14] S.-M. Jung, S.-W. Yun, J.-H. Kim, S.-H. You, J. Park, S. Lee, S.H. Chang, S.C. Chae, S.H. Joo, Y. Jung, J. Lee, J. Son, J. Snyder, V. Stamenkovic, N.M. Markovic, Y.-T. Kim, Selective electrocatalysis imparted by metal–insulator transition for durability enhancement of automotive fuel cells, Nat. Catal. 3 (2020) 639–648, https://doi.org/10.1038/s41929-020-0475-4.

[15] J.H. Kim, E.A. Cho, J.H. Jang, H.J. Kim, T.-H. Lim, I.-H. Oh, J.J. Ko, S.C. Oh, Development of a durable PEMFC startup process by applying a dummy load: I. electrochemical study, J. Electrochem. Soc. 156 (2009) B955, https://doi.org/10.1149/1.3148222.

[16] P.T. Yu, W. Gu, R. Makharia, F.T. Wagner, H.A. Gasteiger, The impact of carbon stability on PEM fuel cell startup and shutdown voltage degradation, ECS Trans. 3 (2006) 797, https://doi.org/10.1149/1.2356199.

[17] J. Durst, A. Lamibrac, F. Charlot, J. Dillet, L.F. Castanheira, G. Maranzana, L. Dubau, F. Mailard, M. Chatenet, O. Lottin, Degradation heterogeneities induced by repetitive start/stop events in proton exchange membrane fuel cell: inlet vs. outlet and channel vs. land, Appl. Catal. B 138–139 (2013) 416–426, https://doi.org/10.1016/j.apcatb.2013.03.021.

[18] C. Qin, J. Wang, D. Yang, B. Li, C. Zhang, Proton exchange membrane fuel cell reversal: a review, Catalysts (2016), https://doi.org/10.3390/catal6120197.

[19] P. Ferreira-Aparicio, A.M. Chaparro, B. Gallardo, M.A. Folgado, L. Daza, Anode degradation effects in PEMFC stacks by localized fuel starvation, ECS Trans. 26 (2010) 257, https://doi.org/10.1149/1.3428996.

[20] B. Randrianarizafy, P. Schott, M. Gerard, Y. Bultel, Modelling carbon corrosion during a PEMFC startup: simulation of mitigation strategies, Energies (2020), https://doi.org/10.3390/en13092338.

[21] J.N. Schwämmlein, P.J. Rheinländer, Y. Chen, K.T. Freyer, H.A. Gasteiger, Anode aging during PEMFC start-up and shut-down: H2-air fronts vs voltage cycles, J. Electro Soc. 165 (2018) F1312, https://doi.org/10.1149/2.0611816jes.

[22] R. Sharma, S.M. Andersen, An opinion on catalyst degradation mechanisms during catalyst support focused accelerated stress test (AST) for proton exchange membrane fuel cells (PEMFCs), Appl. Catal. B 239 (2018) 636–643, https://doi.org/10.1016/j.apcatb.2018.08.045.

[23] A. Kregar, A. Kravos, T. Katrašnik, Methodology for evaluation of contributions of ostwald ripening and particle agglomeration to growth of catalyst particles in PEM fuel cells, Fuel Cells 20 (2020) 487–498, https://doi.org/10.1002/fuce.201900208.

[24] N. Dyantyi, A. Parsons, P. Bujlo, S. Pasupathi, Behavioural study of PEMFC during start-up/shutdown cycling for aeronautic applications, Mater. Renew. Sustain Energy 8 (2019) 4, https://doi.org/10.1007/s40243-019-0141-4.

[25] K.-M. Yin, B.-S. Cheng, K.-W. Chiang, Non-uniform agglomerate cathode catalyst layer model on the performance of PEMFC with consideration of water effect, Renew. Energy 95 (2016) 191–201, https://doi.org/10.1016/j.renene.2016.04.015.

[26] K.K. Karuppanan, A.V. Raghu, M.K. Panthalingal, S. Ramanathan, T. Kumaresan, B. Pullithadathil, Triple phase boundary augmentation in hierarchical, Pt grafted N-doped mesoporous carbon nanofibers for high performance and durable PEM fuel cells, J. Mater. Chem. A 6 (2018) 12768–12781, https://doi.org/10.1039/C8TA02391C.

[27] S. Shahgaldi, J. Hamelin, Improved carbon nanostructures as a novel catalyst support in the cathode side of PEMFC: a critical review, Carbon 94 (2015) 705–728, https://doi.org/10.1016/j.carbon.2015.07.055.

[28] S. Takenaka, H. Matsumori, H. Matsune, E. Tanabe, M. Kishida, High durability of carbon nanotube-supported Pt electrocatalysts covered with silica layers for the cathode in a PEMFC, J. Electrochem. Soc. 155 (2008) B929, https://doi.org/10.1149/1.2952665.

[29] A. Ghosh, S. Basu, A. Verma, Graphene and functionalized graphene supported platinum catalyst for PEMFC, Fuel Cells 13 (2013) 355–363, https://doi.org/10.1002/fuce.201300039.

[30] J. Jung, B. Park, J. Kim, Durability test with fuel starvation using a Pt/CNF catalyst in PEMFC, Nanoscale Res. Lett. 7 (2012) 1–8, https://doi.org/10.1186/1556-276X-7-34.

[31] C. Gupta, P.H. Maheshwari, D. Sachdev, A. Sahu, S. Dhakate, Highly purified CNTs: an exceedingly efficient catalyst support for PEM fuel cell, RSC Adv. 6 (2016) 32258–32271, https://doi.org/10.1039/c5ra28029j.

[32] S. Maass, F. Finsterwalder, G. Frank, R. Hartmann, C. Merten, Carbon support oxidation in PEM fuel cell cathodes, J. Power Sources 176 (2008) 444–451, https://doi.org/10.1016/j.jpowsour.2007.08.053.

[33] S. Sharma, B.G. Pollet, Support materials for PEMFC and DMFC electrocatalysts—a review, J. Power Sources 208 (2012) 96–119, https://doi.org/10.1016/j.jpowsour.2012.02.011.

[34] S.L. Gojković, B.M. Babić, V.R. Radmilovíć, N.V. Krstajić, Nb-doped TiO2 as a support of Pt and Pt–Ru anode catalyst for PEMFCs, J. Electroanal. Chem. 639 (2010) 161–166, https://doi.org/10.1016/j.jelechem.2009.12.004.

[35] L. Chevallier, A. Bauer, S. Cavaliere, R. Hui, J. Roziere, D.J. Jones, Mesoporous nanostructured Nb-doped titanium dioxide microsphere catalyst supports for PEM fuel cell electrodes, ACS Appl. Mater. Interfaces 4 (2012) 1752–1759, https://doi.org/10.1021/am300002j.

[36] T. Ioroi, T. Akita, S.-I. Yamazaki, Z. Siroma, N. Fujiwara, K. Yasuda, Corrosion-resistant PEMFC cathode catalysts based on a Magnéli-phase titanium oxide support synthesized by pulsed UV laser irradiation, J. Electrochem. Soc. 158 (2011) C329, https://doi.org/10.1149/1.3622297.

[37] F. Takasaki, S. Matsuie, Y. Takabatake, Z. Noda, A. Hayashi, Y. Shiratori, K. Ito, K. Sasaki, Carbon-free Pt electrocatalysts supported on SnO2 for polymer electrolyte fuel cells: electrocatalytic activity and durability, J. Electrochem. Soc. 158 (2011) B1270, https://doi.org/10.1149/1.3625918.

[38] P. Zhang, S.-Y. Huang, B.N. Popov, Mesoporous tin oxide as an oxidation-resistant catalyst support for proton exchange membrane fuel cells, J. Electrochem. Soc. 157 (2010) B1163, https://doi.org/10.1149/1.3442371.

[39] V.T.T. Ho, C.-J. Pan, J. Rick, W.-N. Su, B.-J. Hwang, Nanostructured Ti0. 7Mo0. 3O2 support enhances electron transfer to Pt: high-performance catalyst for oxygen reduction reaction, J. Am. Chem. Soc. 133 (2011) 11716–11724, https://doi.org/10.1021/ja2039562.

[40] E. Lee, C. Park, D.W. Lee, G. Lee, H.-Y. Park, J.H. Jang, H.-J. Kim, Y.-E. Sung, Y. Tak, S.J. Yoo, Tunable synthesis of N, C-codoped Ti3+-enriched titanium oxide support for highly durable PEMFC cathode, ACS Catal. 10 (2020) 12080–12090, https://doi.org/10.1021/acscatal.0c02570.

[41] K. Senevirathne, V. Neburchilov, V. Alzate, R. Baker, R. Neagu, J. Zhang, S. Campbell, S. Ye, Nb-doped TiO2/carbon composite supports synthesized by ultrasonic spray pyrolysis for proton exchange membrane (PEM) fuel cell catalysts, J. Power Sources 220 (2012) 1–9, https://doi.org/10.1016/j.jpowsour.2012.07.080.

[42] S. Cavaliere, I. Jiménez-Morales, G. Ercolano, I. Savych, D. Jones, J. Rozière, Highly stable PEMFC electrodes based on electrospun antimony-doped SnO2, ChemElectroChem 2 (2015) 1966–1973, https://doi.org/10.1002/celc.201500330.

[43] P.K. Mohanta, C. Glökler, A.O. Arenas, L. Jörissen, Sb doped SnO2 as a stable cathode catalyst support for low temperature polymer electrolyte membrane fuel cell, Int. J. Hydrog. 42 (2017) 27950–27961, https://doi.org/10.1016/j.ijhydene.2017.06.064.

[44] F. Labbé, E. Disa, Y. Ahmad, K. Guérin, T. Asset, F. Maillard, M. Chatenet, R. Metkemeijer, S. Berthon-Fabry, Tin dioxide coated carbon materials as an alternative catalyst support for PEMFCs: impacts of the intrinsic carbon properties and the synthesis parameters on the coating characteristics, Microporous Mesoporous Mater. 271 (2018) 1–15, https://doi.org/10.1016/j.micromeso.2018.05.019.

[45] J. Song, Z.-F. Huang, L. Pan, J.-J. Zou, X. Zhang, L. Wang, Oxygen-deficient tungsten oxide as versatile and efficient hydrogenation catalyst, ACS Catal. 5 (2015) 6594–6599, https://doi.org/10.1021/acscatal.5b01522, https://doi.org/10.1021/acscatal.5b01522.

[46] Z. Zhang, J. Liu, J. Gu, L. Su, L. Cheng, An overview of metal oxide materials as electrocatalysts and supports for polymer electrolyte fuel cells, Energy Environ. Sci. 7 (2014) 2535–2558, https://doi.org/10.1039/C3EE43886D.

[47] V.O. Makarov, M. Trontelj, Sintering and electrical conductivity of doped WO3, J. Eur. Ceram. 16 (1996) 791–794, https://doi.org/10.1016/0955-2219(95)00204-9.

[48] A. Tseung, K. Chen, Hydrogen spill-over effect on Pt/WO3 anode catalysts, Catal. Today 38 (1997) 439–443, https://doi.org/10.1016/S0920-5861(97)00053-9.

[49] I. Pasti, N. Gavrilov, S. Mentus, Electrocatalytic behavior of Pt/WO3 composite layers formed potentiodynamically on tungsten surfaces, Int. J. Electro Sci. 12 (2017) 5772–5791, https://doi.org/10.20964/2017.06.80.

[50] S. Martínez, M.E. Martins, C. Zinola, Surface metal modifiers for methanol electrooxidation on platinum, molybdenum and tungsten, Int. J. Hydrog. 35 (2010) 5343–5355, https://doi.org/10.1016/j.ijhydene.2010.03.027.

[51] D. Dang, B. Zhao, D. Chen, B.M. deGlee, C. Qu, S. Dai, X. Zeng, J. Liu, Y. Lu, S. Liao, M. Liu, A bi-functional WO3-based anode enables both energy storage and conversion in an intermediate-temperature fuel cell, Energy Stor. Mater. 12 (2018) 79–84, https://doi.org/10.1016/j.ensm.2017.11.016.

[52] J. Chen, C. Chen, M. Qin, B. Li, B. Lin, Q. Mao, H. Yang, B. Liu, Y. Wang, Reversible hydrogen spillover in Ru-WO3-x enhances hydrogen evolution activity in neutral pH water splitting, Nat. Commun. 13 (2022) 5382, https://doi.org/10.1038/s41467-022-33007-3.

[53] M. Szkoda, K. Trzciński, G. Trykowski, M. Łapiński, A. Lisowska-Oleksiak, Influence of alkali metal cations on the photoactivity of crystalline and exfoliated amorphous WO_3-photointercalation phenomenon, Appl. Catal. B 298 (2021), 120527, https://doi.org/10.1016/j.apcatb.2021.120527.

[54] J.H. Kim, Y.J. Lee, Y.S. Jang, J.N. Jang, D.H. Kim, B.C. Song, D.H. Lee, S.N. Kwon, M. Hong, The effect of Ar plasma bombardment upon physical property of tungsten oxide thin film in inverted top-emitting organic light-emitting diodes, Org. Electron. 12 (2011) 285–290, https://doi.org/10.1016/j.orgel.2010.10.023.

[55] Q. Li, S. Li, O. Ajouyed, C. Chen, Y. Zhou, C. Li, S. Niu, H. Yi, J. Huo, S. Wang, Room temperature plasma enriching oxygen vacancies of WO3 nanoflakes for photoelectrochemical water oxidation, J. Alloy. Compd. 816 (2020), 152610, https://doi.org/10.1016/j.jallcom.2019.152610.

[56] H. Liang, Z. Cao, C. Xia, F. Ming, W. Zhang, A.-H. Emwas, L. Cavallo, H. N. Alshareef, Tungsten blue oxide as a reusable electrocatalyst for acidic water oxidation by plasma-induced vacancy engineering, CCS Chem. 3 (2021) 1553–1561, https://doi.org/10.31635/ccschem.020.202000325.

[57] M. Gillet, C. Lemire, E. Gillet, K. Aguir, The role of surface oxygen vacancies upon WO3 conductivity, Surf. Sci. 532 (2003) 519–525, https://doi.org/10.1016/S0039-6028(03)00477-1.

[58] N.E. Richey, C. De Paula, S.F. Bent, Understanding chemical and physical mechanisms in atomic layer deposition, J. Chem. Phys. 152 (2020), 040902, https://doi.org/10.1063/1.5133390.

[59] J. Ahn, C. Ahn, S. Jeon, J. Park, Atomic layer deposition of inorganic thin films on 3D polymer nanonetworks, Appl. Sci. 9 (2019) 1990, https://doi.org/10.3390/app9101990.

[60] H. Kim, Atomic layer deposition of metal and nitride thin films: current research efforts and applications for semiconductor device processing, J. Vac. Sci. Technol. B 21 (2003) 2231–2261, https://doi.org/10.1116/1.1622676.

[61] C.-C. Ting, C.-H. Liu, C.-Y. Tai, S.-C. Hsu, C.-S. Chao, F.-M. Pan, The size effect of titania-supported Pt nanoparticles on the electrocatalytic activity towards methanol oxidation reaction primarily via the bifunctional mechanism, J. Power Sources 280 (2015) 166–172, https://doi.org/10.1016/j.jpowsour.2015.01.081.

[62] B.-R. Koo, K.-H. Kim, H.-J. Ahn, Switching electrochromic performance improvement enabled by highly developed mesopores and oxygen vacancy defects of Fe-doped WO3 films, Appl. Surf. Sci. 453 (2018) 238–244, https://doi.org/10.1016/j.apsusc.2018.05.094.

[63] Y. Liu, L. Kong, X. Guo, J. Xu, S. Shi, L. Li, Surface oxygen vacancies on WO3 nanoplate arrays induced by Ar plasma treatment for efficient photoelectrochemical water oxidation, J. Phys. Chem. Solids 149 (2021), 109823, https://doi.org/10.1016/j.jpcs.2020.109823.

[64] D. Migas, V. Shaposhnikov, V. Rodin, V. Borisenko, Tungsten oxides. I. effects of oxygen vacancies and doping on electronic and optical properties of different phases of WO 3, J. Appl. Phys. 108 (2010), 093713, https://doi.org/10.1063/1.3505688.

[65] M. Gerosa, F. Gygi, M. Govoni, G. Galli, The role of defects and excess surface charges at finite temperature for optimizing oxide photoabsorbers, Nat. Mater. 17 (2018) 1122–1127, https://doi.org/10.1038/s41563-018-0192-4.

[66] S. Rahimnejad, J.H. He, W. Chen, K. Wu, G.Q. Xu, Tuning the electronic and structural properties of WO 3 nanocrystals by varying transition metal tungstate precursors, RSC Adv. 4 (2014) 62423–62429, https://doi.org/10.1039/C4RA10650D.

[67] A. Kregar, T. Katrašnik, Theoretical analysis of particle size re-distribution due to Ostwald ripening in the fuel cell catalyst layer, Open Phys. J. 17 (2019) 779–789, https://doi.org/10.1515/phys-2019-0081.

[68] J. Song, Q. Ye, K. Wang, Z. Guo, M. Dou, Degradation investigation of electrocatalyst in proton exchange membrane fuel cell at a high energy efficiency, Molecules 26 (2021) 3932, https://doi.org/10.3390/molecules26133932.

[69] A. Vasilyev, Modelling polymer electrolyte membrane fuel cells for dynamic reliability assessment, Loughborough University, 2019.

[70] R. Ebrahim, M. Yeleuov, A. Issova, S. Tokmoldin, A. Ignatiev, Triple-phase boundary and power density enhancement in thin solid oxide fuel cells by controlled etching of the nickel anode, Nanoscale Res. Lett. 9 (2014) 286, https://doi.org/10.1186/1556-276X-9-286.

[71] H.M. Barkholtz, L. Chong, Z.B. Kaiser, T. Xu, D.-J. Liu, Enhanced performance of non-PGM catalysts in air operated PEM-fuel cells, Int. J. Hydrogen 41 (2016) 22598–22604, https://doi.org/10.1016/j.ijhydene.2016.08.193.

[72] R. Yeetsorn, Y. Maiket, W. Kaewmanee, The observation of supercapacitor effects on PEMFC–supercapacitor hybridization performance through voltage degradation and electrochemical processes, RSC Adv. 10 (2020) 13100–13111, https://doi.org/10.1039/D0RA00468E.

[73] T.R. Ralph, S. Hudson, D.P. Wilkinson, Electrocatalyst stability in PEMFCs and the role of fuel starvation and cell reversal tolerant anodes, ECS Trans. 1 (2006) 67, https://doi.org/10.1149/1.2214545.

[74] G. Nagy, R. Schiller, Hydrogen in tungsten bronzes: mechanism of hydrogen intercalation, Int. J. Hydrog. 14 (1989) 567–572, https://doi.org/10.1016/0360-3199(89)90115-8.

[75] H.-E. Kim, S. Shin, H. Lee, Pt-IrOx catalysts immobilized on defective carbon for efficient reversal tolerant anode in proton exchange membrane fuel cells, J. Catal. 395 (2021) 404–411, https://doi.org/10.1016/j.jcat.2021.01.028.
[76] I. Jang, I. Hwang, Y. Tak, Attenuated degradation of a PEMFC cathode during fuel starvation by using carbon-supported IrO2, Electrochim. Acta 90 (2013) 148–156, https://doi.org/10.1016/j.electacta.2012.12.034.
[77] L. Wang, Z. Zhu, W. Ren, X. Zhang, J. Zhang, P. Chen, C. Xu, High performance bifunctional Pt/C-RuO2/Ti3C2Tx catalyst for reversal-tolerant anodes of polymer electrolyte membrane fuel cells, ACS Appl. Energy Mater. 5 (2022) 13990–13996, https://doi.org/10.1021/acsaem.2c02598.
[78] C.-W. Roh, H.-E. Kim, J. Choi, J. Lim, H. Lee, Monodisperse IrOx deposited on Pt/C for reversal tolerant anode in proton exchange membrane fuel cell, J. Power Sources 443 (2019), 227270, https://doi.org/10.1016/j.jpowsour.2019.227270.
[79] R. Azimirad, N. Naseri, O. Akhavan, A. Moshfegh, Hydrophilicity variation of WO3 thin films with annealing temperature, J. Phys. D. Appl. Phys. 40 (2007) 1134, https://doi.org/10.1088/0022-3727/40/4/034.
[80] G. Li, Y. Wang, J. Bi, X. Huang, Y. Mao, L. Luo, H. Hao, Partial oxidation strategy to synthesize WS2/WO3 heterostructure with enhanced adsorption performance for organic dyes: Synthesis, modelling, and mechanism, Nanomaterials 10 (2020) 278, https://doi.org/10.3390/nano10020278.
[81] C. Chen, T.F. Fuller, Modeling of H2O2 formation in PEMFCs, Electrochim. Acta 54 (2009) 3984–3995, https://doi.org/10.1016/j.electacta.2009.02.021.
[82] E. Endoh, Highly durable MEA for PEMFC under high temperature and low humidity conditions, ECS Trans. 3 (2006) 9, https://doi.org/10.1149/1.2356118.